Symmetric and Antisymmetric Components of Polar-Amplified Warming

SPENCER A. HILL,[a] NATALIE J. BURLS,[b] ALEXEY FEDOROV,[c,d] AND TIMOTHY M. MERLIS[e]

[a] *Lamont-Doherty Earth Observatory, Columbia University, Palisades, New York*
[b] *Department of Atmospheric, Oceanic, and Earth Sciences, Center for Ocean-Land-Atmosphere Studies, George Mason University, Fairfax, Virginia*
[c] *Department of Earth and Planetary Sciences, Yale University, New Haven, Connecticut*
[d] *LOCEAN/IPSL, Sorbonne University, Paris, France*
[e] *Department of Atmospheric and Oceanic Sciences, McGill University, Montreal, Quebec, Canada*

(Manuscript received 16 December 2020, in final form 1 July 2022)

ABSTRACT: CO_2-forced surface warming in general circulation models (GCMs) is initially polar amplified in the Arctic but not in the Antarctic—a largely hemispherically antisymmetric signal. Nevertheless, we show in CESM1 and 11 LongRunMIP GCMs that the hemispherically symmetric component of global-mean-normalized, zonal-mean warming (T^*_{sym}) under 4 × CO_2 changes weakly or becomes modestly more polar amplified from the first decade to near-equilibrium. Conversely, the antisymmetric warming component (T^*_{asym}) weakens with time in all models, modestly in some including FAMOUS, but effectively vanishing in others including CESM1. We explore mechanisms underlying the robust T^*_{sym} behavior with a diffusive moist energy balance model (MEBM), which given radiative feedback parameter (λ) and ocean heat uptake ($\mathscr{O}$) fields diagnosed from CESM1 adequately reproduces the CESM1 T^*_{sym} and T^*_{asym} fields. In further MEBM simulations perturbing λ and $\mathscr{O}$, T^*_{sym} is sensitive to their symmetric components only, and more to that of λ. A three-box, two-time-scale model fitted to FAMOUS and CESM1 reveals a curiously short Antarctic fast-response time scale in FAMOUS. In additional CESM1 simulations spanning a broader range of forcings, T^*_{sym} changes modestly across 2–16 × CO_2, and T^*_{sym} in a Pliocene-like simulation is more polar amplified but likewise approximately time invariant. Determining the real-world relevance of these behaviors—which imply that a surprising amount of information about near-equilibrium polar amplification emerges within decades—merits further study.

KEYWORDS: Climate change; Surface temperature; Climate models

1. Introduction

Climatological zonal-mean surface temperatures decrease from the equator toward both poles, a hemispherically symmetric signature much larger than the antisymmetric deviations therefrom. By symmetric or antisymmetric we refer to the average or difference, respectively, of each latitude with its mirror about the equator: for a given field χ, $\chi(\varphi) = \chi_{sym}(\varphi) + \chi_{asym}(\varphi)$, where φ is latitude, $\chi_{sym} \equiv (1/2)[\chi(\varphi) + \chi(-\varphi)]$ is the symmetric component, and $\chi_{asym} \equiv (1/2)[\chi(\varphi) - \chi(-\varphi)]$ is the antisymmetric component. Figure 1a illustrates this via a preindustrial control simulation in the Community Earth System Model version 1.0.4 (henceforth CESM1) general circulation model (GCM) whose formulation will be described below. Evidently, the symmetric annual-mean forcing of insolation and approximately symmetric forcing of CO_2 and other well-mixed greenhouse gases outweigh the antisymmetric components of Earth's ocean basins, water vapor, orography, sea ice, clouds, and atmospheric and oceanic circulations.

Conversely, CO_2-forced zonal-mean surface warming—henceforth simply T—starts out appreciably antisymmetric: prevailing Southern Ocean upwelling (e.g., Armour et al. 2013; Marshall et al. 2015) impedes Antarctic warming for decades (likely reinforced by resulting changes in local lapse rates and clouds; Senior and Mitchell 2000; Rugenstein et al. 2020), while weakly negative to slightly positive radiative feedbacks in northern high latitudes (e.g., Stuecker et al. 2018) among other processes (Feldl et al. 2017; Russotto and Biasutti 2020; Henry et al. 2021) promote Arctic warming. This fast response typically gives way to a more symmetric warming pattern over subsequent centuries (Held et al. 2010), with Antarctic warming partially catching up to the Arctic in century-scale CMIP5 (Andrews et al. 2015) and CMIP6 (Dong et al. 2020) simulations. On longer time scales, polar amplification is comparable in the two hemispheres in multimillennial simulations in fully coupled GCMs (e.g., Danabasoglu and Gent 2009; Li et al. 2013; Rugenstein et al. 2019) and in runs to equilibrium in slab-ocean GCMs (e.g., Manabe et al. 1991; Armour et al. 2013) and diffusive moist energy balance models (MEBMs) (e.g., Merlis and Henry 2018; Armour et al. 2019). Figure 1b illustrates these behaviors via T and T_{sym} from an abrupt 4 × CO_2 simulation in CESM1 over each of four time periods (years 1–10, 21–100, 701–800, and 2901–3000): T and T_{sym} differ markedly in the first decade when T_{asym} is largest but gradually become more similar, with $T \approx T_{sym}$ and $T_{asym} \approx 0$ to first approximation in the final period.

On millennial time scales changes in deep-ocean circulation become relevant (and can be non-monotonic, cf. Jansen et al. 2018), perturbing the prevailing antisymmetric transport of

Hill's current affiliation: Program in Atmospheric and Oceanic Sciences, Princeton University, Princeton, New Jersey.

Corresponding author: Spencer Hill, spencerh@princeton.edu

DOI: 10.1175/JCLI-D-20-0972.1

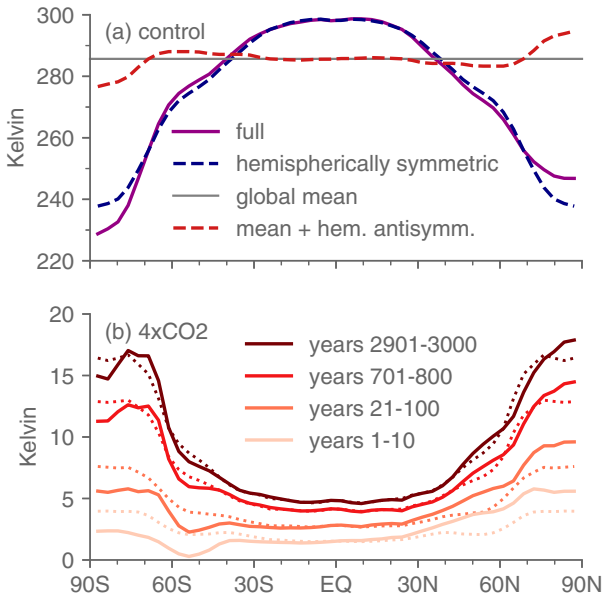

FIG. 1. (a) Climatological annual-mean, zonal-mean surface air temperature in a preindustrial control simulation, the hemispherically symmetric component thereof, the global mean thereof, and the global mean plus the hemispherically antisymmetric component, as indicated in the legend. The simulation was performed in a low-resolution configuration of CESM version 1.0.4, with results averaged over years 701–800. (b) Anomalous zonal-mean surface air temperature in an abrupt 4 × CO_2 simulation in the same model, averaged over four time periods as indicated in the legend. Solid curves are the full fields, and dotted curves are the corresponding symmetric component. Both panels have units in K.

heat from the southern to the Northern Hemisphere by the Atlantic meridional overturning circulation. For example, in a 3000-yr GCM simulation with perturbed cloud albedos yielding a surface climate resembling the early Pliocene (~4 Ma), a Pacific meridional overturning circulation emerges after ~1500 years, increasing the heat convergence into the Northern Hemisphere (Burls et al. 2017).

Nevertheless, past studies indicate that T normalized by its global average—henceforth T^*—partially collapses toward a shared pattern at different time scales (cf. Fig. 4a of Armour et al. 2013). Such pattern scaling (e.g., Tebaldi and Arblaster 2014) also largely holds for zonally varying surface temperature responses across CO_2 values [e.g., Heede et al. (2020), though there is also considerable evidence for state-dependent climate sensitivity; e.g., Rohrschneider et al. (2019)]. Essentially, the present study combines pattern scaling and the symmetric/antisymmetric decomposition for T under 4 × CO_2, arguing that GCM-simulated T^*_{sym} changes surprisingly little from the first decade to near-equilibrium while T^*_{asym} weakens markedly. Taken at face value, this would imply that polar amplification (defined as the ratio of polar cap to globally averaged warming) at near-equilibrium in a given GCM can be meaningfully constrained from a single decade of forced change.

We found these behaviors somewhat inadvertently in the aforementioned 4 × CO_2 simulation in CESM1 (which is described along with the other models and methodological choices in section 2), and this manuscript constitutes an attempt to better understand them. To assess their robustness, we analyze 11 additional GCMs from the LongRunMIP (Rugenstein et al. 2019) repository (section 3). To clarify their underlying physical mechanisms, we use an MEBM to first emulate the results from CESM1 and then identify the predominant factors determining T^*_{sym} (section 4). To better understand their differences across these GCMs, we fit a three-box, two-time-scale model to two end-members of these 12, CESM1 and FAMOUS (section 5). And to assess their relevance across different forcings, we analyze 2, 8, and 16 × CO_2 simulations and the aforementioned Pliocene-like simulation in CESM1 (section 6). We conclude with summary and discussion (section 7), including comparison to the more traditional approach of studying polar amplification in either cap separately, potential means of further testing these behaviors, and implications for the real climate system. We view these results as suggestive, rather than definitive, and hope they motivate further studies of the hemispherically symmetric and antisymmetric components of surface warming and what controls them in models and the real world.

2. Methods

a. *LongRunMIP and CESM1 4 × CO_2 simulations*

LongRunMIP (Rugenstein et al. 2019) comprises increased-CO_2 simulations from CMIP5-class GCMs spanning from one thousand to several thousand years. We analyze 11 of the 12 available with ≥1000-yr integrations under 4 × CO_2, which are listed in Table 1. CESM104 from LongRunMIP was omitted because it is nearly the same as the above-noted CESM1 that we analyze separately. Nine of the LongRunMIP models ran under an abrupt 4 × CO_2 and two under a 1% increase per year to 4 × CO_2. The latter two (ECHAM5MPIOM and MIROC32) also ran shorter abrupt 4 × CO_2 simulations, and so for the first century when forcing and global-mean warming are modest under 1% yr^{-1} we use the abrupt 4 × CO_2 simulation, switching to the 1% to 4 × CO_2 simulation for subsequent periods. Output was available regridded to a common 2.5° × 2.5° grid (cf. Table 2 of Rugenstein et al. 2019).

We include with the LongRunMIP models the 3000-yr 4 × CO_2 simulation in CESM1 referred to in the Introduction. This is version 1.0.4 of the model in its low-resolution configuration (Shields et al. 2012). It consists of the Community Atmosphere Model, version 4 with its spectral dynamical core truncated at T31 resolution (~3.75° × 3.75°) and with 26 vertical levels coupled to the Parallel Ocean Program version 2 (POP2) with ~3° horizontal resolution and 60 vertical levels.

We focus on temporal averages over four time periods (similar to those of Armour et al. 2013): years 1–10 and 21–100 (during which both the atmosphere and ocean are rapidly responding), 701–800 (during which the atmosphere is in a nearly statistically steady state but the ocean remains slowly varying), and 2901–3000 (at which time the deep ocean has nearly equilibrated). All 12 GCMs extend through year 800

TABLE 1. Details of the LongRunMIP models and simulations used. (from left to right) Model name following Rugenstein et al. (2019) conventions, control simulation duration in years, simulation for which data over years 701–800 is taken, and simulation for which data over years 2901–3000 are taken (or "none" if not available for any simulation in that model).

Model	Control duration (years)	701–800 simulation	2901–3000 simulation
CCSM3	1530	4 × CO_2	None
CNRMCM61	2000	4 × CO_2	None
ECHAM5MPIOM	100	1% 4 × CO_2	1% 4 × CO_2
FAMOUS	3000	4 × CO_2	4 × CO_2
GISSE2R	5225	4 × CO_2	4 × CO_2
HadCM3L	1000	4 × CO_2	None
HadGEM2	239	4 × CO_2	None
IPSLCM5A	1000	4 × CO_2	None
MIROC32	680	1% 4 × CO_2	None
MPIESM11	2000	4 × CO_2	4 × CO_2
MPIESM12	1237	4 × CO_2	None

and 5 through year 3000. We refer to the final period as near-equilibrium, recognizing that the climate response would likely meaningfully evolve beyond three millennia in most models given the deep ocean's multimillennial, diffusive equilibration time scale (Jansen et al. 2018); the box model in section 5 highlights this.

We account for climate drift in each model's preindustrial control simulation as follows. For the 11 LongRunMIP GCMs, for each time period we compute anomalies as the difference between the 4 × CO_2 simulation and the control at that time period if the control simulation extends that long. Otherwise, we subtract an average over the entire control simulation. For CESM1, drift in the control simulation is modest relative to the forced temperature responses, and so for convenience we report anomalies in all periods as differences with the control averaged over years 701–800. All major results presented are insensitive to reasonable methodological choices regarding control drift.

The five GCMs extending to year 3000 include the three farthest on the ends of the full 12-GCM distribution at years 701–800: FAMOUS on one end (highest global-mean warming, and second-weakest changes in both the symmetric and antisymmetric polar amplification indices defined below), versus GISSE2R and CESM1 (respectively, lowest and third lowest mean warming, largest and second-largest increase in symmetric amplification, and second-largest and largest decrease in antisymmetric amplification) on the other. Most likely then this subset usefully approximates the range generated by all 12 models had the others also run to year 3000.

b. *Moist energy balance model*

To clarify the processes determining the GCM T^*_{sym} and T^*_{asym} behaviors of our interest, we use a highly idealized diffusive moist energy balance model (MEBM). MEBMs have been a useful simplified modeling framework for emulating the warming pattern in comprehensive GCMs (Hwang et al. 2011; Bonan et al. 2018) and developing theory for the spatial pattern of warming (Flannery 1984; Rose et al. 2014; Roe et al. 2015; Merlis and Henry 2018; Russotto and Biasutti 2020), and we pursue both purposes here. In short, the MEBM is forced with a realistic, time-invariant estimate of 4 × CO_2 radiative forcing and, for each of the four selected time periods, input fields taken from the CESM1 4 × CO_2 simulation—either unmodified or perturbed as will be described in section 4.

The MEBM's governing equation is

$$\mathscr{C}\partial_t T(\varphi) = \mathscr{F}(\varphi) + \lambda(\varphi)T(\varphi) - \mathscr{O}(\varphi) + \mathscr{D}\nabla^2 h(\varphi), \qquad (1)$$

where $\mathscr{C}$ is the surface layer heat capacity, T is anomalous surface temperature, $\mathscr{F}$ is the imposed radiative forcing, λ is the radiative feedback parameter, $\mathscr{O}$ is the anomalous net surface flux (signed positive downward; also known as ocean heat uptake), $\mathscr{D}$ is the spatially uniform diffusivity, and h is surface moist static energy (MSE). In words, the time tendency of the heat content of the surface layer (LHS) is determined by the combined effect of (RHS terms, left to right) the imposed radiative forcing (which is identical across all MEBM runs), a radiative restoring term encompassing the net effect of all TOA radiative feedbacks and that varies linearly with the surface temperature anomaly, an imposed ocean heat uptake field, and the convergence of the anomalous column-integrated MSE flux, approximated as downgradient diffusion of surface MSE. The MEBM numerics and the calculations of each RHS term are conventional and detailed in the Appendix.

c. *Additional CESM1 simulations under different forcings*

To assess how robust the behaviors of T^*_{sym} and T^*_{asym} are to forcings other than 4 × CO_2, we also analyze instantaneous 2, 8, and 16 × CO_2 simulations in CESM1, as well as the Pliocene-like simulation mentioned in the introduction (Burls and Fedorov 2014a). In the latter, atmospheric composition remains preindustrial, but—only in shortwave radiative transfer calculations—liquid water path is decreased by 240% poleward of 15° in both hemispheres, while both ice and liquid water paths are increased by 60% within 15°S–15°N. This increases the albedo of the deep tropical band, promoting local cooling, but decreases the albedo elsewhere, promoting warming (Burls and Fedorov 2014b; Fedorov et al. 2015). Each spans 3000 years.

d. *Physical meaning of symmetric/antisymmetric decomposition*

Arguably, the decomposition of T into a sum and difference of its mirror values about the equator—though always permissible mathematically—gains physical meaning only to the extent that mirror latitudes influence one another. Otherwise, if for example each latitude was in local radiative-convective equilibrium independent of all others, summing or differencing about the equator merely convolves two independent signals. But it is well understood that perturbed atmospheric and oceanic energy flux divergences do strongly influence polar amplification (e.g., Alexeev and Jackson 2013; Armour et al. 2019; Henry et al. 2021), mitigating this concern, at least over sufficiently long time scales.

Nevertheless, a corollary is that this decomposition becomes physically meaningful only beyond the time scale over which a given latitude plausibly influences its mirror. For example, while Previdi et al. (2020) argue convincingly that Arctic amplification emerges in a matter of months after imposed CO_2 forcing, for our purposes this Arctic signal is unlikely communicated to the opposite pole on such a subannual time scale. Shin and Kang (2021) show that, in an aquaplanet GCM with radiative forcing confined to one hemisphere's extratropics, local warming is communicated to the opposite polar cap through a multistep circulation adjustment, manifesting in surface warming over ~5–10 years. For non-aquaplanets, zonal asymmetries plausibly yield teleconnections mediated by Rossby waves that could potentially transmit the signal across the tropics more rapidly (Ding et al. 2014); nevertheless we take the Shin and Kang (2021) result as a posteriori justification for our choice of the first decade as the earliest and shortest period analyzed.

Though a few prior studies have applied the symmetric/antisymmetric decomposition to related properties of the atmospheric energy budget, to our knowledge none have applied it to surface warming itself. Frierson and Hwang (2012) use the antisymmetric component of zonal-mean net energetic forcing of the atmosphere to interpret tropical precipitation and atmospheric energy fluxes under doubled CO_2. In terms of hemispheric averages, observations and GCMs exhibit considerable symmetry in top-of-the-atmosphere (TOA) albedo climatologically (Voigt et al. 2013; Stephens et al. 2015) and in GCMs under hemispherically antisymmetric external forcing (Voigt et al. 2014).

e. *Amplification indices*

As quantitative bulk measures of T^*_{sym} and T^*_{asym}, we start with conventional indices of polar amplification: Arctic amplification is the ratio of T averaged over 60°–90°N to its global-mean, and Antarctic amplification the same but using 60°–90°S. We then define symmetric (PA_{sym}) and antisymmetric (PA_{asym}) polar amplification indices as the average or half the difference of the Arctic and Antarctic indices, respectively.

3. 4 × CO_2 results in GCMs

Figure 2 shows the 4 × CO_2-forced T^*, T^*_{sym}, and T^*_{asym} fields for each period specified above in 6 of the 12 GCMs; the remaining six are shown in Fig. 3. Printed in each T^* panel are that model's global-mean warming (henceforth $\overline{T}$) for each time period, in each T^*_{sym} panel that model's PA_{sym} for each period and its percentage change from the first decade to the last available period, and in each T^*_{asym} panel that model's PA_{asym} for each period and its first-to-last percentage change. Across models, $\overline{T}$ spans 2.0–3.9 K in the first decade and increases monotonically afterward in all models, with values 3.0–9.0 K in years 21–100, 4.3–12.7 K in years 701–800, and 4.8–13.8 K in years 2901–3000. In the first decade only, in all 12 T^* minimizes over the Southern Ocean. For nearly all models and latitudes south of ~40°S, T^* increases monotonically in time. The evolution of northern extratropical warming varies more across models, but in most T^* decreases with time over much of ~40°–70°N.

The T^*_{sym} is polar-amplified in all models and time periods, and by eye it either changes modestly or becomes somewhat more polar amplified with time. Quantitatively, PA_{sym} spans 1.16–1.67 across models in the initial decade, 1.23–1.79 in years 21–100, 1.31–1.96 in years 701–800, and 1.49–2.05 in years 2901–3000. In one outlier, GISSE2R, it increases from the first decade to the last available period by 34%, and unique to this model the T^*_{sym} field is similar for the first two periods but then seems to jump to one shared by the latter two periods. In the remaining 11 GCMs, PA_{sym} changes by ≤8% in 6 models (with negative change in FAMOUS, −5%, and HadCM3L, −6%), and increases by ≤22% in the remaining 5 models. As such, we consider a weak change to modest increase in PA_{sym} from decadal to millennial time scales under 4 × CO_2 to be an empirically robust response across these models.

The T^*_{asym} field reflects greater Arctic than Antarctic warming initially but also a weakening in time of that difference in all models. Quantitatively, PA_{asym} is positive in the first decade in all models, spanning 0.89–1.65, and then decreases monotonically in 10 of 12 models, spanning 0.69–1.35 in years 21–100, −0.02 to +0.98 in years 701–800, and −0.15 to +0.73 in years 2901–3000. The two negative values, both in CESM1, indicate that Antarctic warming exceeds Arctic warming. The fractional change in PA_{asym} from the first decade to the last available period is negative in all models but varies considerably, −16% to −109%. We consider a modest to complete reduction in PA_{asym} to likewise be a robust response.[1]

Given these two robust responses, empirically each model's PA_{sym} in the initial decade provides a nontrivial albeit approximate lower bound on its near-equilibrium PA_{sym} value—and for models in which T^*_{asym} weakens strongly leaving $T^* \approx T^*_{sym}$ at near-equilibrium, this extends to polar amplification in each hemispheric cap. By eye, indeed the full T^*_{sym} field changes less with time in nearly all models than does T^* and less still than T^*_{asym}. We may quantify this using the ratio PA_{asym}/PA_{sym}, which ranges from −0.01 in CESM1 to +0.64

[1] We are using the term "robust" here in two slightly different senses. For PA_{sym}, the robustness refers more to the cross-model spread being small than to the sign of the response (though the sign is shared by 10 of 12 models). For PA_{asym}, the robustness refers to the sign, with all 12 models simulating a decrease with time, despite a much wider range of magnitudes in that decrease.

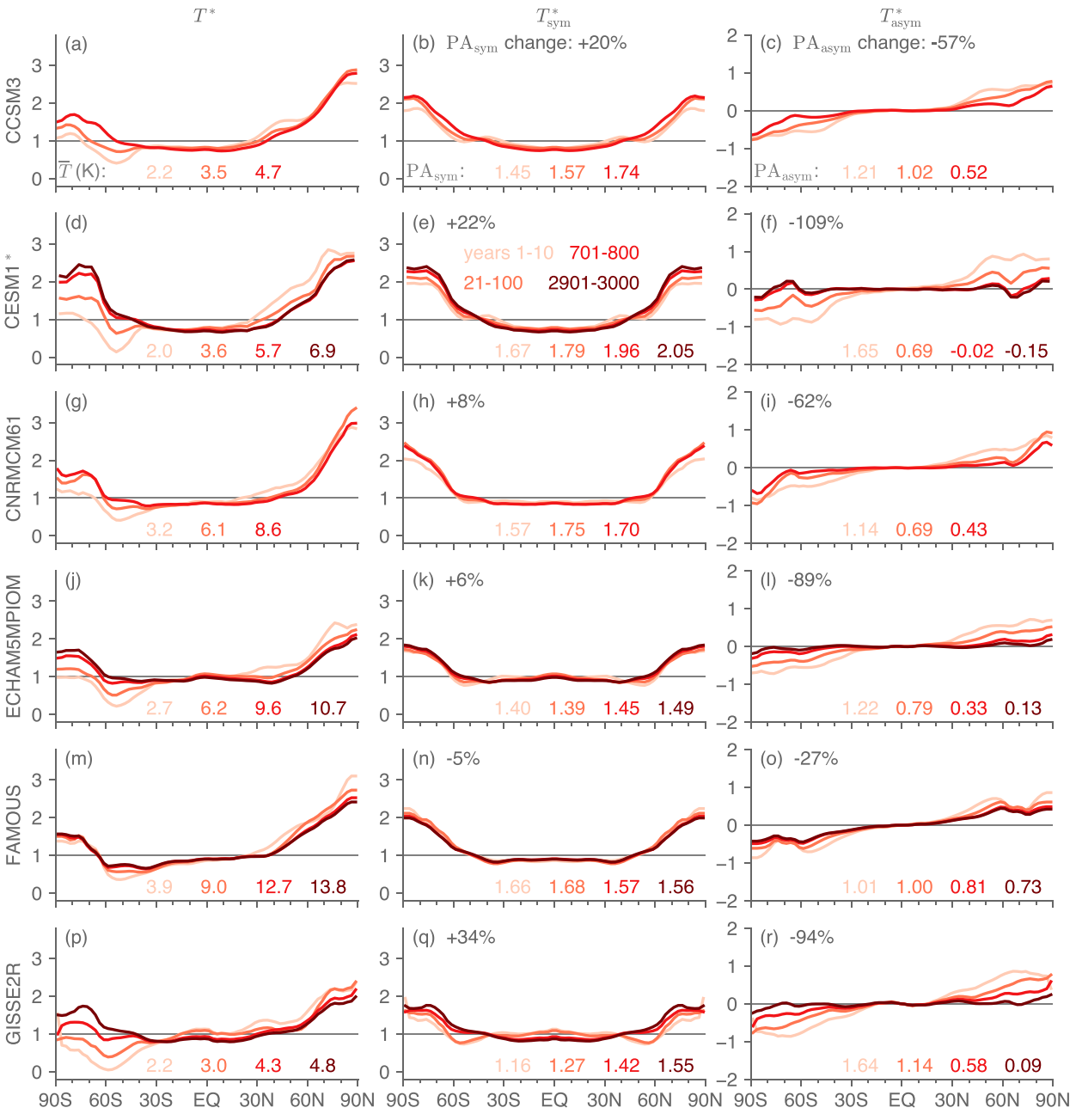

FIG. 2. For 4 × CO_2 simulations in 6 of the 12 GCMs analyzed: (left) full, (center) hemispherically symmetric component, and (right) antisymmetric component of zonal-mean surface air temperature change in years 1–10, 21–100, 701–800, and if available years 2901–3000, with each period as indicated in the legend in (e). Printed values at the bottom of each panel are (left) the mean warming during that period, (center) the symmetric polar amplification index for that period, and (right) the northern minus Southern Hemisphere polar amplification index for that period. Values at the top of each panel in the center column are the fractional change in the symmetric polar amplification index from the first to the last period, and at the top of each panel the right column are the same but for the northern–southern difference. (d)–(f) For CESM1, the asterisk signifies that these simulations are not from LongRunMIP (unlike the 11 other models). The remaining six models are shown in Fig. 3.

in IPSLCM5A for years 701–800 and −0.07 in CESM1 to 0.47 in FAMOUS for years 2901–3000. It becomes less positive between these periods in all five models run to years 2901–3000, at which point it is ≤10% in magnitude in CESM1, ECHAM5MPIOM, and GISSE2R. From Fig. 2 the correspondence between the initial T^*_{sym} and final T^* fields is debatable for the two whose PA_{asym}/PA_{sym} ratios are not small (0.42 in MPIESM11 and 0.47 in FAMOUS), intermediate for GISSE2R (recall its aforementioned jump in T^*_{sym} after the first century), but clear for CESM1 and ECHAM5MPIOM.

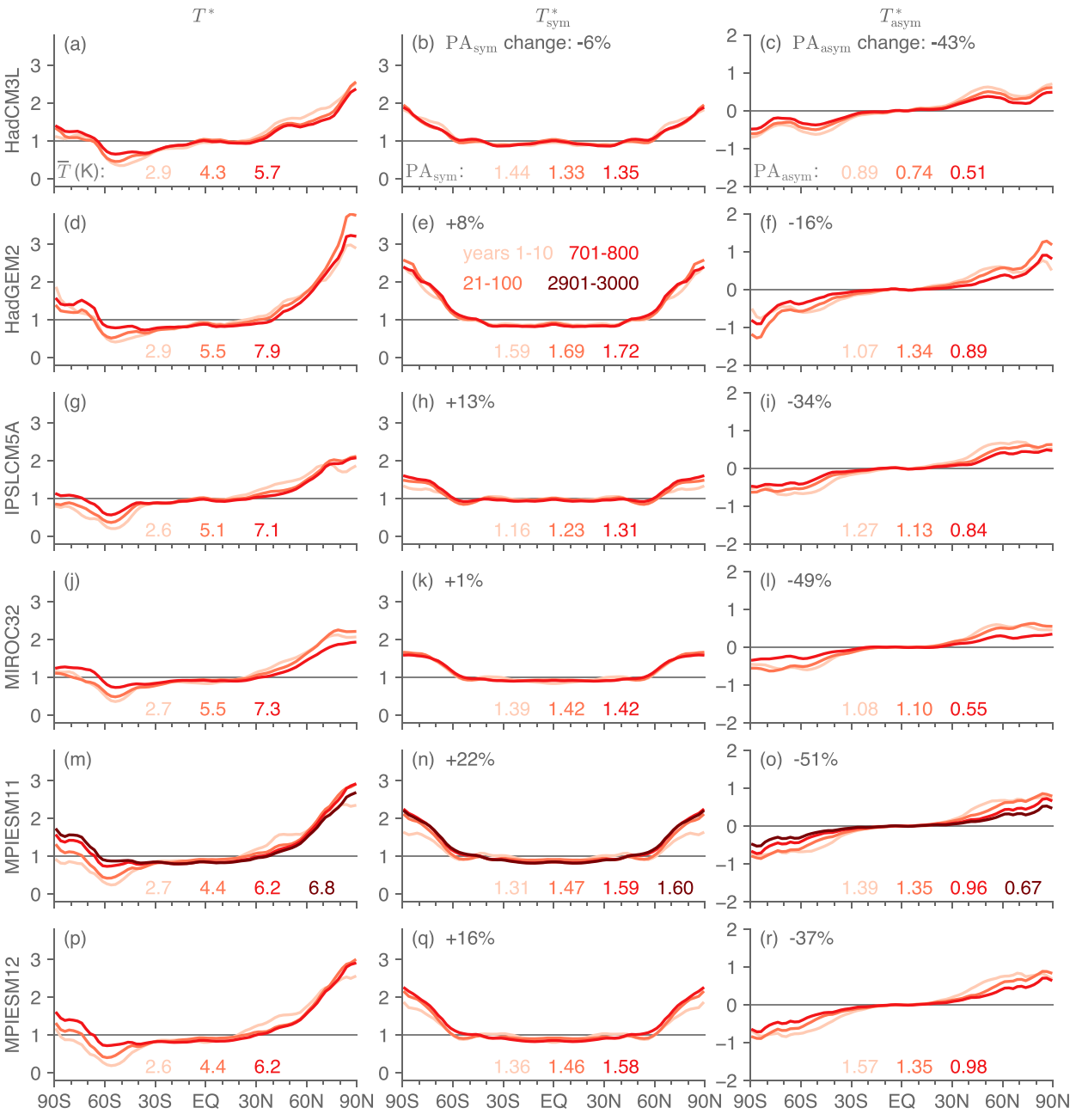

FIG. 3. As in Fig. 2, but for the remaining six GCMs.

Having established these behaviors in full-physics GCMs, we turn to better understanding them via two simpler models: first with an MEBM to clarify the physical mechanisms underlying the robust T^*_{sym} and T^*_{asym} behaviors, and then with a box model to explore the GCM diversity in PA_{sym} and PA_{asym} evolutions.

4. Moist energy balance model

Figure 4 shows T, T^*, T^*_{sym}, and T^*_{asym} for each time period in the CESM1 4 × CO_2 simulation and the corresponding MEBM simulations; recall the MEBM simulations differ from one another only in the time period in CESM1 from which the radiative feedback parameter (λ) and ocean heat uptake (OHU; $\mathscr{O}$) were diagnosed as detailed in appendix. The MEBM captures the mean warming ($\overline{T}$ is within 0.3 K of CESM1 for all four periods) and raw warming patterns reasonably well and therefore T^*—in particular the gradual, modest increase in polar amplification in T^*_{sym} and the steady but severe weakening of T^*_{asym}. High-latitude warming gradients are insufficiently sharp (a common feature of MEBMs with uniform diffusivity, e.g., Bonan et al. 2018), especially in the Arctic, yielding a moderate low bias in the Arctic

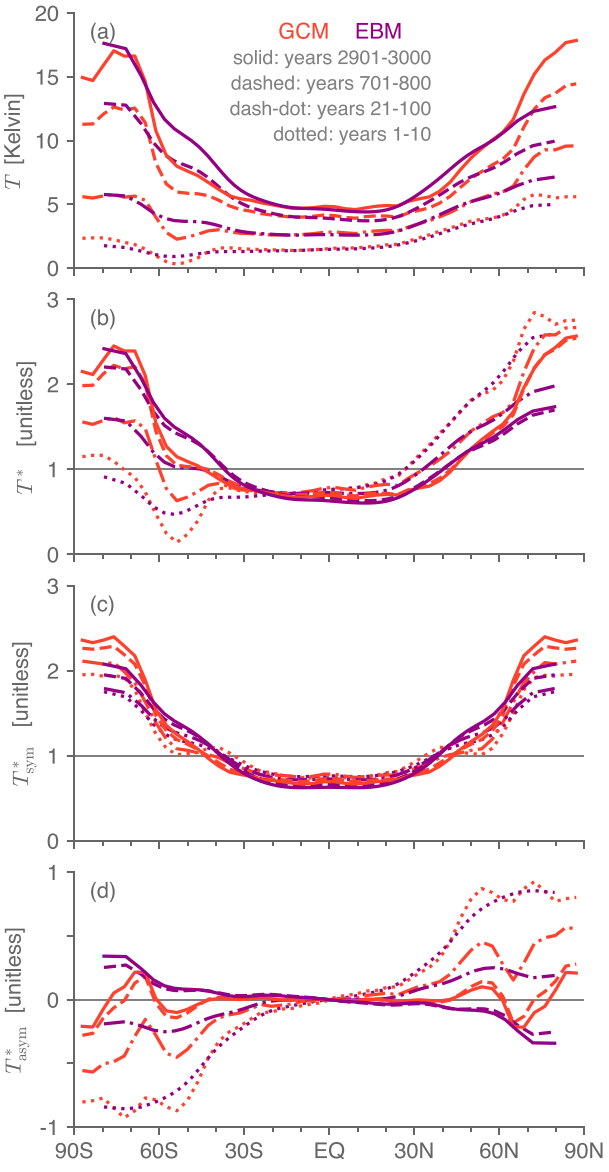

FIG. 4. Surface air temperature response in the CESM1 4 × CO_2 simulation at the four selected time periods and in the moist energy balance model simulations meant to reproduce the CESM1 4 × CO_2 simulation at each of those time periods, as indicated by the text in (a). Panels show different temperatures: (a) raw (in K), (b) mean-normalized (unitless), (c) mean-normalized symmetric component (unitless), and (d) mean-normalized antisymmetric component (unitless). Note differing vertical axis spans in each panel.

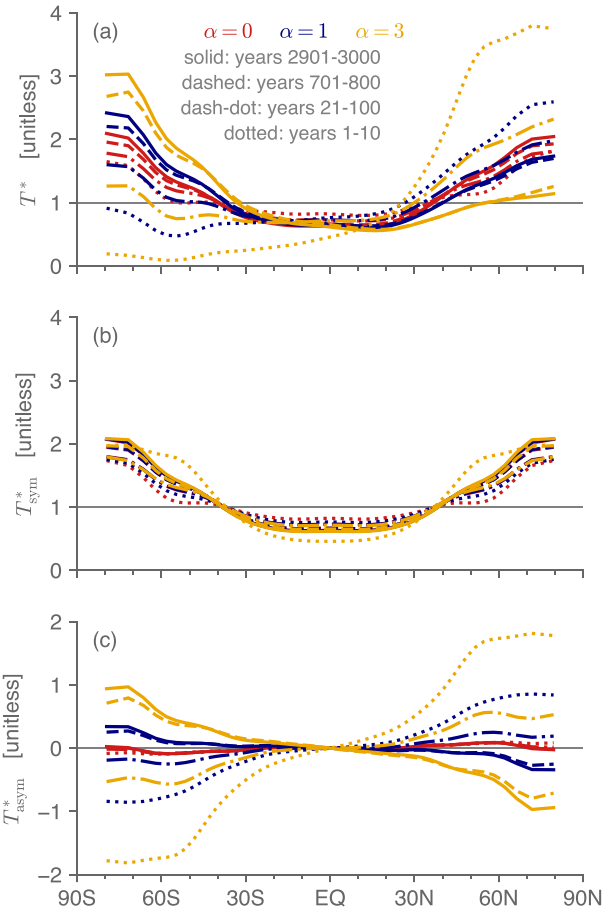

FIG. 5. Mean-normalized (a) full, (b) symmetric, and (c) antisymmetric surface air temperature anomaly fields in MEBM simulations with the antisymmetric components of the radiative feedback parameter and ocean heat uptake fields multiplied by the factor α, with red curves for $\alpha = 0$, blue for $\alpha = 1$ (i.e., unchanged), and dark yellow for $\alpha = 3$. Dotted, dash–dotted, dashed, and solid lines correspond to years 1–10, 21–100, 701–800, and 2901–3000, respectively, of the CESM1.0.4 abrupt 4 × CO_2 simulation. Note that the vertical axis range is identical in (a) and (b), but not in (c), while the vertical axis spacing is identical in all three panels.

amplification index by years 2901–3000 (1.62 in the MEBM versus 1.97 in CESM1) but less so for the Antarctic index due to compensating within-region T biases (2.16 in the MEBM versus 2.13 in CESM1 for years 2901–3000). More importantly, the MEBM suitably captures the fractional change in both PA_{sym} and PA_{asym} from CESM1: the MEBM PA_{asym} decreases by −132% (from 0.83 to −0.27, versus −109% in CESM1), and its PA_{sym} increases by 19% (from 1.59 to 1.89, versus 22% in CESM1). As such, we can use the MEBM to further probe the underlying physical mechanisms.

To test the role of anti-symmetries in λ and $\mathscr{O}$, Fig. 5 shows T^*, T^*_{sym}, and T^*_{asym} from simulations with λ and $\mathscr{O}$ replaced by λ_{sym} and $\mathscr{O}_{sym}$. The resulting symmetric warming patterns (red curves) closely resemble the original ones (blue curves).[2] Quantitatively, $\overline{T}$ changes from the full MEBM simulation by ≤0.3 K and PA_{sym} by 0.04 or 3% in all periods. In a complementary simulation, the antisymmetric components are amplified rather than suppressed: we set $\lambda^* = \lambda_{sym} + \alpha\lambda_{asym}$, where

[2] Modest anti-symmetries stem from the radiative forcing and the climatological surface air temperature used to compute $\partial_T q_{sat}$; in additional simulations with these also symmetrized (not shown), the warming pattern is very similar to the symmetric pattern shown.

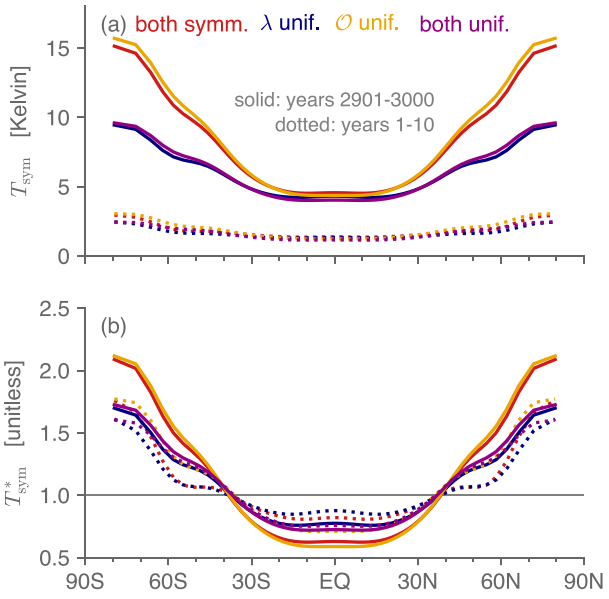

FIG. 6. Surface air temperature response in MEBM simulations corresponding to years 1–10 (dotted curves) and years 2901–3000 (solid curves) of the CESM1 4 × CO_2 simulation, shown either (a) raw (in K) or (b) mean-normalized (unitless). Colors correspond to simulations with (red) both λ and $\mathscr{O}$ symmetrized but not uniform, (blue) λ set to its global-mean value at all latitudes, (yellow) $\mathscr{O}$ set to its global-mean value at all latitudes, or (purple) both $\mathscr{O}$ and λ set to their global-mean values at all latitudes.

λ^* is the modified feedback parameter, $\mathscr{O}$ is modified likewise, and $\alpha = 3$ (yellow curves in Fig. 5). Although this strongly modifies T and T^*_{asym} in all periods, after the first decade $\overline{T}$ changes by at most 0.7 K, qualitatively the T^*_{sym} pattern changes weakly, and quantitatively PA_{sym} changes by $\leq$0.03. These results suggest that T^*_{sym} and PA_{sym} are largely insensitive to λ_{sym} and $\mathscr{O}_{asym}$, leading us to focus henceforth on λ_{sym} and $\mathscr{O}_{sym}$.

To test the role of the spatial patterns of λ_{sym} and $\mathscr{O}_{sym}$, Fig. 6 shows T_{sym} and T^*_{sym} in simulations with λ and $\mathscr{O}$ replaced at all latitudes by their global averages, $\overline{\lambda}$ and $\overline{\mathscr{O}}$, respectively (purple curves).[3] To focus on the biggest-picture behaviors, we restrict to simulations corresponding to the first decade (when $\overline{\lambda} = -2.0\ W\ m^{-2}\ K^{-1}$ and $\overline{\mathscr{O}} = 3.9\ W\ m^{-2}$) and to years 2901–3000 (when $\overline{\lambda} = -1.3\ W\ m^{-2}\ K^{-1}$ and $\overline{\mathscr{O}} = -0.4\ W\ m^{-2}$ W m^{-2}). With uniform $\mathscr{O}$ and λ, warming is reduced in the extratropics especially and globally averaged ($\overline{T}$ is 0.2 K cooler for the first decade and 1.7 K cooler for years 2901–3000), and T^* is less polar-amplified and changes less in time: PA_{sym} is reduced from 1.54 to 1.51 (a 2% decrease) in the first decade and from 1.89 to 1.60 (a 15% decrease) in years 2901–3000. In other words, the meridional patterns of λ_{sym} and $\mathscr{O}_{sym}$ together make warming stronger in the mean and more polar-amplified compared to if they were uniform.

To distinguish the contributions of λ_{sym} versus $\mathscr{O}_{sym}$, Fig. 6 also includes simulations with only one of λ or $\mathscr{O}$ made uniform. For each time period, T_{sym} of the original simulation more closely resembles the uniform-$\mathscr{O}$ than uniform-λ simulation, which in turn more closely resembles the both-uniform simulation. Quantitatively, in years 2901–3000 $\overline{T}$ is 0.2 K warmer than the $\lambda = \lambda_{sym}$, $\mathscr{O} = \mathscr{O}_{sym}$ case when $\mathscr{O}$ is uniform versus 1.7 K cooler when λ is uniform; PA_{sym} is slightly increased with uniform $\mathscr{O}$, from 1.89 to 1.93 (2%) versus more strongly decreased with uniform λ, from 1.89 to 1.55 (−18%). In other words, the evolving spatial pattern of λ_{sym} (along with the mean of $\mathscr{O}$) acts to increase warming in the global mean and make it more polar-amplified, and these influences are stronger than those of the evolving spatial pattern of $\mathscr{O}_{sym}$ (along with the mean of λ) in determining T_{sym} and T^*_{sym}.

To interpret this strong influence of λ_{sym}, Fig. 7 shows λ, λ_{sym}, and λ_{asym} for each time period (as well as, for completeness in interpreting the various MEBM simulations, the corresponding $\mathscr{O}$ fields and those of the time-invariant radiative forcing). λ is negative at nearly all latitudes in all periods and is generally more negative in the tropics than high latitudes. In the first decade it has a pronounced global minimum of $\sim -6\ W\ m^{-2}\ K^{-1}$ near 50°S, just equatorward of the global maximum in $\mathscr{O}$ driven by Southern Ocean upwelling. After the first decade, it becomes less stabilizing in the global average (increasing climate sensitivity, cf. Armour et al. 2013) and at most latitudes south of ~10°N at least somewhat. But the largest regional change is a vanishing of the sharp global minimum in λ by years 21–100. With much weaker changes in the Northern Hemisphere, these signals project onto λ_{sym} as well. λ_{sym} therefore becomes less stabilizing in the extratropics than tropics after the first decade, acting to increase polar amplification with time.[4]

Summarizing: the MEBM captures the CESM1 warming patterns reasonably well when forced with the latter's λ and $\mathscr{O}$ fields; for T_{sym} and PA_{sym} to good approximation only the symmetric components of λ and $\mathscr{O}$ matter; of these the predominant influence on the time evolution of T_{sym} and PA_{sym} is that of λ_{sym}; and physically this stems from an initial strongly stabilizing radiative feedback over the Southern Ocean that vanishes after the first decade, making λ_{sym} become preferentially less stabilizing at high compared to low latitudes, increasing polar amplification. We infer that changes in T^*_{sym} are modest to the extent that changes in the spatial pattern of λ_{sym} are themselves modest.

5. Box model of amplification indices

Having explored the mechanisms underlying the robust responses across the GCMs, we now investigate the cross-GCM discrepancies via a three-box, two-time-scale model applied to two of the end-member GCMs noted above, CESM1 and

[3] In the MEBM, there is no true distinction between OHU and the radiative forcing, and so imposing the mean OHU uniformly can be equally conceptualized as reducing the global-mean radiative forcing.

[4] Strictly speaking, the λ_{sym} signal sits just outside our chosen Antarctic region boundary of 60°S. But the diffusive MSE transport in the MEBM clearly communicates this signal to the adjacent polar cap.

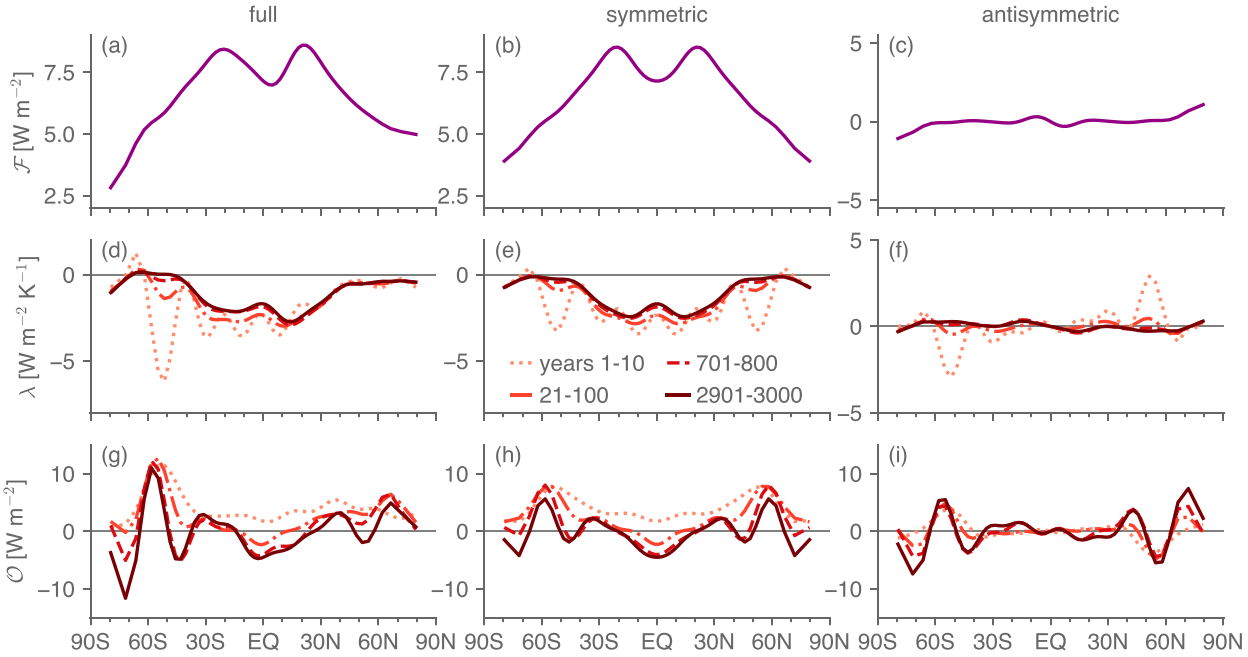

FIG. 7. (a)–(c) Radiative forcing ($\mathscr{F}$; units: W m^{-2}), (d)–(f) radiative feedback parameter (λ; units: W m^{-2} K^{-1}), and (g)–(i) ocean heat uptake ($\mathscr{O}$, signed positive downward into the ocean; units: W m^{-2}) fields used for the MEBM simulations for each time period, with radiative forcing constant across time periods. Columns show (left) The full fields, (center) the hemispherically symmetric component, and (right) the hemispherically antisymmetric component. For each row, the left and center panels have the same vertical axis ranges, and the right column has the same vertical axis spacing as the other columns (except for the bottom row), but not the same range.

FAMOUS[5] (Smith et al. 2008). Our three-box model is an extension of the well-known two-time-scale box model for global-mean warming (Held et al. 2010; Geoffroy et al. 2013; Rohrschneider et al. 2019) to region-mean warming (see also Geoffroy and Saint-Martin 2014) in the Arctic (60°–90°N), Antarctic (60°–90°S), and lower latitudes (60°S–60°N). Recalling that CESM1 has the second-least mean warming, second-most positive change in $\mathrm{PA_{sym}}$ (+22%), and most negative change in $\mathrm{PA_{asym}}$ (−109%) whereas FAMOUS has the most mean warming, second-least positive (−5%) change in $\mathrm{PA_{sym}}$, and second-least negative (−27%) change in $\mathrm{PA_{asym}}$, this diagnosis of the regional warming time scales points toward potential causes of the spread in T^*_{sym} and T^*_{asym} across the GCMs.

The physical basis for the two-time-scale model is the presence of a shallow, relatively rapidly evolving ocean layer and a deeper, more slowly evolving deep ocean (e.g., Held et al. 2010). The two-time-scale solution for a given region is given by

$$T(t) = T_{\mathrm{eq}}[a_{\mathrm{f}}(1 - e^{-t/\tau_{\mathrm{f}}}) + a_{\mathrm{s}}(1 - e^{-t/\tau_{\mathrm{s}}})], \qquad (2)$$

where T_{eq} is the equilibrium temperature change, τ_{f} and τ_{s} are the fast and slow warming time scales, respectively, and a_{f} and a_{s} are the fractional contributions of the fast and slow responses, respectively, to the equilibrium warming, with $a_{\mathrm{f}} + a_{\mathrm{s}} = 1$. For each model and region, we fit T_{eq}, a_{f}, a_{s}, τ_{f}, and τ_{s} of (2) via nonlinear least squares (using the "curve_fit" function of the scipy Python package; Virtanen et al. 2020) applied to annual-mean time series of the region-mean surface temperature anomaly. Although they do not appear explicitly, note that the ocean heat uptake and anomalous atmospheric energy flux divergence fields implicitly influence the values of all five parameters. The resulting best-fit parameter values are listed in Table 2, and the GCM regional-mean, annual-mean time series (smoothed via a 10-year running mean) and corresponding box-model solutions are shown both raw and mean-normalized in Fig. 8.

For CESM1, T_{eq} is slightly higher for the Antarctic (17.8 K) than Arctic (15.1 K), both of which are ~3 times higher than for lower latitudes (5.8 K). The fast response time scales for the Arctic (9.4 years) and lower latitudes (12.7 years) are comparable and an order of magnitude less than the Antarctic time scale (85.3 years). Equilibrium warming is weighted fairly evenly between the fast and slow responses (a_{f} = 0.59, 0.48, and 0.60 for the Arctic, Antarctic, and lower latitudes, respectively). The slow response time scales are all millennial—2223, 2564, and 1065 years for the Arctic, Antarctic, and lower latitudes, respectively. The two-time-scale fit captures the overall evolution for each region fairly well, though with too sharp a shoulder after the initial decades for the Arctic and lower latitudes (Fig. 8a). CESM1 also exhibits considerable centennial-time-scale variability particularly after ~1800 years (roughly coinciding with the emergence of the Pacific meridional overturning circulation in the Pliocene-like

[5] Compare with Table 1 of Rugenstein et al. (2020), FAMOUS is also an outlier in that the equilibrium warming estimated for CO_2-doubling differs nearly twofold whether $2 \times CO_2$ or $4 \times CO_2$ simulations are used (4.40 and 8.55 K, respectively).

TABLE 2. Best-fit values of the five parameters in the two-time-scale model for the abrupt 4 × CO_2 simulations in CESM1 and in FAMOUS for each of the three regions of our box model and for the global mean. Units are in K for T_{eq} and years for τ_f and τ_s; a_f and a_s are dimensionless.

	CESM1					FAMOUS				
	T_{eq} (K)	τ_f (years)	a_f	τ_s (years)	a_s	T_{eq} (K)	τ_f (years)	a_f	τ_s (years)	a_s
Arctic	15.1	9.4	0.59	2223	0.41	26.4	15.9	0.78	471	0.22
Antarctic	17.8	85.3	0.48	2564	0.52	16.1	15.3	0.71	588	0.29
Lower lats	5.8	12.7	0.60	1065	0.40	12.3	14.1	0.66	433	0.34
Globe	7.1	15.9	0.58	1188	0.42	13.5	14.5	0.68	445	0.32

simulation; Burls et al. 2017). For the fast response, the separation of the Antarctic time scale from the Arctic and lower latitudes is evident. For the slow response, it is evident that both caps would continue warming nontrivially beyond year 3000, which after all is only ~1.2–1.3 times their slow response time scales. The global-mean-normalized time series (Fig. 8c) show the initial strong Arctic amplification and the Antarctic subsequently catching up by around ~500–600 years.

The two-time-scale fit is even better for FAMOUS than for CESM1 (Fig. 8b) and highlights the striking result that the Antarctic fast response time scale is slightly *shorter* than the Arctic's—τ_f = 14.1, 15.9, and 15.3 years for lower latitudes, Arctic, and Antarctic, respectively—unlike CESM1 and counter to physical intuition given the retarding influence of Southern Ocean upwelling. The predicted equilibrium warming is over 10 K higher in the Arctic (26.4 K) than Antarctic (16.1 K), which in turn is less than 4 K warmer than the lower latitudes (12.3 K). It is also weighted more toward the fast than slow response for all three regions, with a_f = 0.78, 0.71, and 0.66 for the Arctic, Antarctic, and lower latitudes, respectively. With comparable time scales and weightings for the fast response but much larger equilibrium warming in the Arctic, initial decades feature much greater Arctic than Antarctic warming. The slow response time scale is similar for lower latitudes and Arctic (433 and 471 years, respectively), and moderately longer for the Antarctic (588 years). As such, the Antarctic continues warming somewhat longer than the rest of the globe, which moderately weakens the antisymmetric amplification. Still, the Antarctic slow time scale is within ~25%–35% of the others.

These values motivate a first approximation for FAMOUS in which both time scales and their relative weights are uniform across regions. Let T_N, T_S, and T_L, respectively, be the Arctic, Antarctic, and low-latitude box temperature anomaly, and let γ be the ratio of the low-latitude surface area to the surface areas of either polar cap (with 60°S/N borders, $\gamma \approx 6.5$).

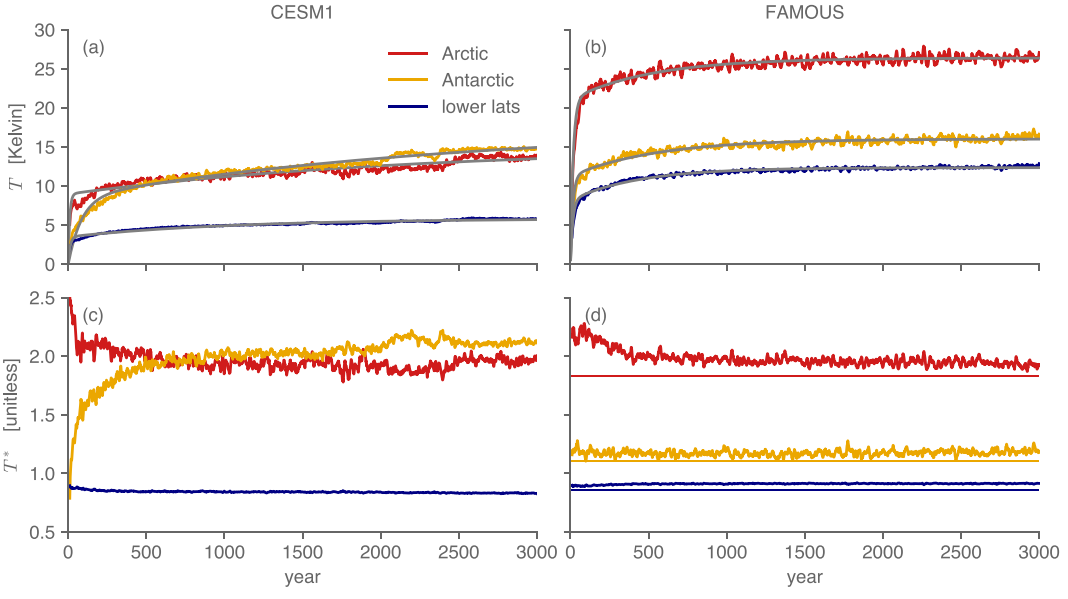

FIG. 8. Time series of 10-yr running mean of Arctic (red), Antarctic (yellow), and low-latitude (blue) box-average temperatures in the abrupt 4 × CO_2 simulation in (a),(c) CESM1 and (b),(d) FAMOUS. Overlain gray curves are the fits from the simple two-layer box model for each region. Rows show (top) raw fields and (bottom) the same time series but each normalized by the global-mean warming. The plot in (d) also includes as thin horizontal lines the predictions from the box model under the approximation of horizontally uniform fast and slow warming time scales, as described in the text.

Then $\overline{T} = (T_S + \gamma T_L + T_S)/(\gamma + 2)$, and the amplification indices are $PA_{sym} = (T_N + T_S)/2\overline{T}$ and $PA_{asym} = (T_N - T_S)/2\overline{T}$. Denoting the equilibrium temperature anomalies $T_{eq,i}$ for $i \in \{N, L, S\}$ and assuming each of τ_f, τ_s, a_f, and a_s do not vary across the three boxes, the global-mean temperature anomaly is

$$\overline{T}(t) = \frac{T_{eq,S} + \gamma T_{eq,L} + T_{eq,N}}{\gamma + 2} \times [a_f(1 - e^{-t/\tau_f}) + a_s(1 - e^{-t/\tau_s})]. \quad (3)$$

The global-mean-normalized temperature anomaly in each region is then

$$\frac{T_i(t)}{\overline{T}(t)} = \frac{(\gamma + 2)T_{eq,i}}{T_{eq,S} + \gamma T_{eq,L} + T_{eq,N}}, \qquad i \in (N, L, S). \quad (4)$$

This is independent of time. Therefore so too are PA_{sym} and PA_{asym}—imperfect for the −27% decrease in PA_{asym} but capturing the modest −6% change in PA_{sym} well. Figure 8c shows the global-mean-normalized warming for each region for FAMOUS along with their predicted values from (4). The simple approximation (4) is biased low for each region, but in reasonable agreement with (4) the FAMOUS time series vary modestly in time, at most for the Arctic by ~10% over the 3000 years.

Summarizing, for CESM1 there are three relevant time scales. In the initial decades, the Arctic warms rapidly but not the Antarctic, yielding large values of both PA_{sym} and PA_{asym}. The fast Antarctic warming transpires over subsequent decades to centuries, increasing PA_{sym} but weakening PA_{asym}. Over subsequent millennia, the slow responses emerge continuing to warm both polar caps, comparably to one another but more than lower latitudes, further increasing PA_{sym} while decreasing PA_{asym}. For FAMOUS, a surprisingly short time scale of Antarctic warming combined with much greater Arctic than Antarctic (or low-latitude) equilibrium warming combine to keep changes in both PA_{sym} and PA_{asym} modest from decadal to millennial time scales. These results show that the preferential initial Arctic versus Antarctic amplification, though robust, can arise via rather different processes in different GCMs.

6. Results across CO_2 levels and a Pliocene-like simulation in CESM1

Though bounding a GCM's near-equilibrium PA_{sym} from a short integration would be useful, our ultimate concern is what can be inferred for the real climate system, for which an instantaneous quadrupling of CO_2 is not directly relevant to anthropogenic warming—in which the CO_2 increase is gradual and (one dearly hopes) remains well below a quadrupling—nor those paleoclimate states for which non-CO_2 forcings are of first-order importance. We therefore now present CESM1 simulations at 2–16 × CO_2 and the Pliocene-like simulation; these address the sensitivity of the results to CO_2 amount and to a strongly meridionally patterned, non-CO_2 forcing but do not directly address the issue of gradual rather than abrupt forcings, which we return to in the concluding discussion section below.

The left column of Fig. 9 shows T, T^*, T^*_{sym}, and T^*_{asym} for each perturbed CO_2 simulation and time period. For T, warming occurs at all latitudes, is weakest and relatively flat at low latitudes, and increases nearly monotonically moving from low to high latitudes (peaking in the Southern Hemisphere from ~65°S for 2 × CO_2 to ~80°S for 16 × CO_2). Across CO_2 levels and time periods, low-latitude warming ranges from ~2 to ~11 K, peak SH high-latitude warming from ~6 to ~25 K, and peak NH warming at the North Pole from ~7 to ~34 K. $\overline{T}$ spans across periods 0.8–3.6, 2.0–6.9, 3.5–9.8, and 5.2–13.6 K for 2, 4, 8, and 16 × CO_2, respectively. For T^*, the patterns are most similar across CO_2 amounts and time scales in the tropics, moderately so in the northern extratropics, and least of all in the southern extratropics. The Arctic amplification index decreases in time, and the Antarctic index increases, in all cases, both with the largest changes under 2 × CO_2 (from 2.50 in the first decade to 1.97 for years 2901–3000 for the Arctic and from 0.75 to 2.57 for the Antarctic).

The T^*_{sym} is quite similar across CO_2 values and time periods, though least for the 2 × CO_2 first and last periods. For all CO_2 values the pattern becomes slightly more polar amplified in time, with low-latitude values decreasing and high-latitude values increasing. Quantitatively, PA_{sym} spans 1.62–2.29 across all CO_2 amounts and time scales (respectively occurring in years 1–10 and 2901–3000 under 2 × CO_2). In other words, PA_{sym} starts smallest and ends up largest in 2 × CO_2, increasing less with time (from the first to last period, by +41%, 22%, 18%, and 8% for 2–16×, respectively), and to a smaller near-equilibrium value (2.29, 2.05, 1.96, and 1.83, respectively) as CO_2 increases. The value of T^*_{asym} varies appreciably across the four time scales, reflecting the gradual catching-up of Antarctic and Southern Ocean warming with (and for 2 and 4 × CO_2, surpassing) the initially rapid Arctic warming. Similar to PA_{sym} but with signs reversed, PA_{asym} is most positive in the first decade under 2 × CO_2 but then becomes most negative at near-equilibrium (0.9 and −0.3 in the first decade and years 2901–3000, respectively), and it decreases less with time as CO_2 increases (from the first to last period, by −132%, −109%, −81%, and −72% for 2–16×, respectively). Particularly in the first century, T^*_{asym} groups together more by time scale than by CO_2 value (cf. curves with the same line markings to those with the same color). This likely reflects the intrinsic time scales of the underlying physical processes—no matter how large a radiative forcing, prevailing Southern Ocean upwelling inhibits initial local surface warming, while the deep ocean equilibration that acts to homogenize subsurface warming between the hemispheres takes millennia.

The right column of Fig. 9 shows T, T^*, T^*_{sym}, and T^*_{asym} in the Pliocene-like simulation, with the corresponding 2–16 × CO_2 values underlain for comparison. Recalling that cloud albedo is increased 15°S–15°N and decreased poleward thereof, the warming is unsurprisingly more polar-amplified in all time periods than under CO_2. Mean warming is 1.6, 3.2, 4.6, and 5.5 K, respectively, in the four periods. The first decade's mean-normalized fields, with T^*_{sym} particularly cool at low latitudes and T^*_{asym} large near the poles, sit separate from the three subsequent periods across which they are very similar. As for CO_2, the Arctic amplification index is initially large (3.2) and the Antarctic

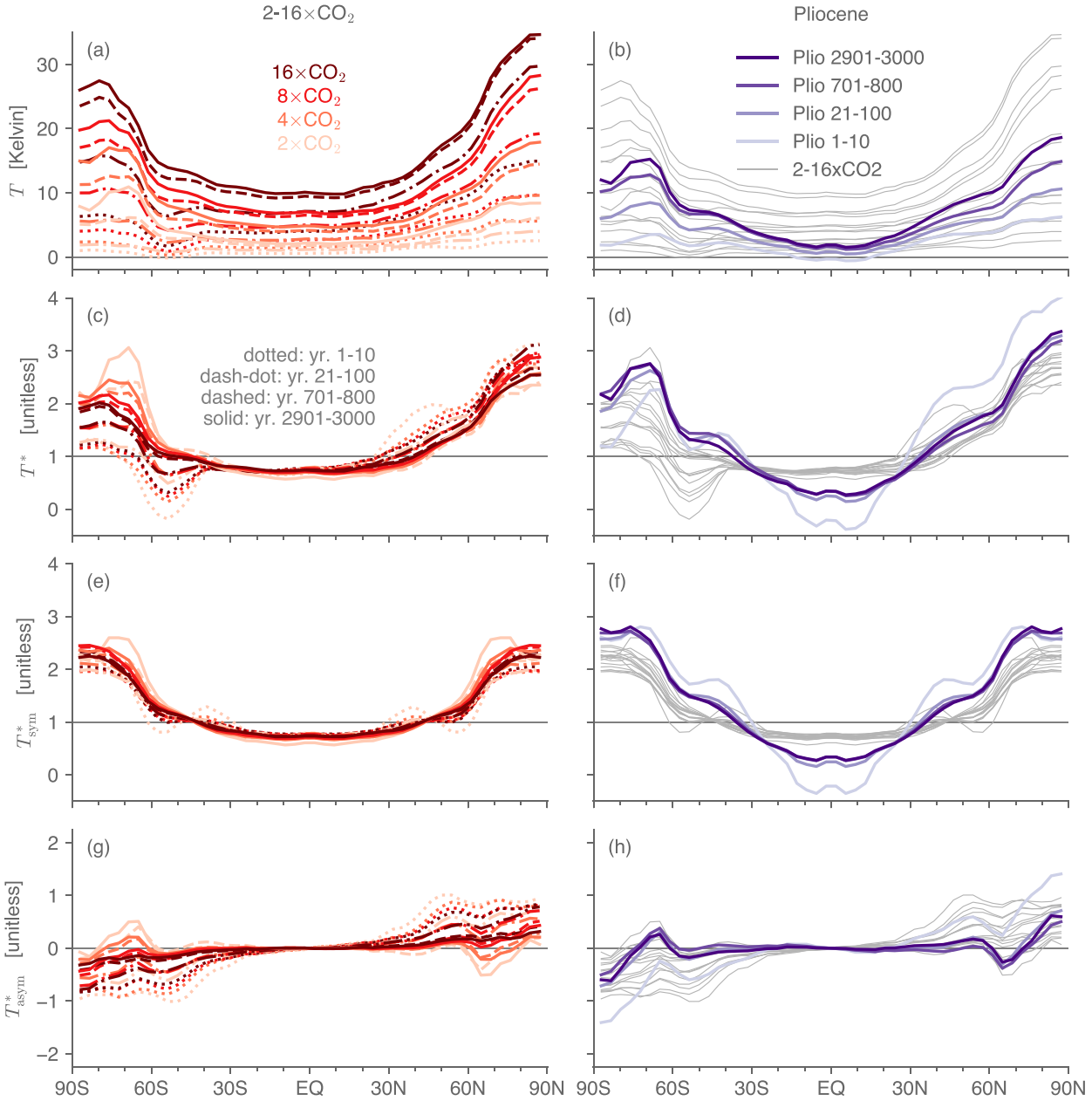

FIG. 9. Zonal-mean surface warming in (a),(c),(e),(g) 2, 4, 8, and 16 × CO_2 simulations and (b),(d),(f),(h) the Pliocene-like simulation in CESM1. For CO_2, colors are according to the legend in (a) and line styles according to the legend in (c). For the Pliocene-like simulation, the legend is in (b). Shown are (a),(b) raw warming (in K) and the mean-normalized (c),(d) full field, (e),(f) symmetric component, and (g),(h) antisymmetric component. Vertical axis range is identical in (c)–(f), which also have the same vertical axis spacing as (g) and (h).

index smaller (1.9), but by years 21–100 they are nearly the same: 2.4, 2.2, and 2.4 for the Arctic in the three time periods versus 2.3, 2.4, and 2.4, respectively. The T^*_{sym} is more polar-amplified than the CO_2 cases, but like the CO_2 cases it changes modestly in time. Quantitatively, PA_{sym} = 2.6 in the first decade and 2.4 in the remaining three periods, and PA_{asym} = 0.6 in the first decade and essentially vanishes (within −0.1 to +0.1) thereafter.

Summarizing, across CO_2 values in CESM1 the T^*_{sym} pattern is qualitatively consistent, more so than T^*_{asym} due to relative Arctic warming increasing with CO_2. Quantitatively, PA_{sym} modestly increase with time for each CO_2 amount, but less so as CO_2 increases. Similarly, PA_{asym} decreases (i.e., becomes more negative) in time at all CO_2 amounts, but less so as CO_2 increases. Under the polar-amplified forcing of the Pliocene-like simulation, unsurprisingly surface warming is

itself more polar-amplified than for the quasi-uniform CO_2 forcing, but it changes weakly after the first decade. These results help to contextualize the cross-model spread in PA_{sym} and PA_{asym} under $4 \times CO_2$. They suggest that the fractional changes in PA_{sym} and PA_{asym} depend to a nontrivial extent on the forcing magnitude itself—consider that CESM1's 41% increase in PA_{sym} under $2 \times CO_2$ is appreciably larger than all 12 GCMs under $4 \times CO_2$ (at most +34%). Similarly, the 72%–132% range in the decrease of PA_{asym} for CESM1 across CO_2 amounts is not vastly smaller than the range across LongRunMIP models under $4 \times CO_2$ of 16%–109%. At the same time, consistency of PA_{sym} and PA_{asym} at least after the first decade is even stronger under more meridionally structured forcing.

7. Conclusions

a. Summary

We decompose the zonal-mean surface air temperature response to abrupt CO_2 quadrupling from decadal to millennial time scales into hemispherically symmetric and antisymmetric components in 12 GCMs—11 from LongRunMIP (Rugenstein et al. 2019) plus a low-resolution version of CESM1.0.4. Normalized by the contemporaneous global-mean warming, the symmetric warming component at a given time differs considerably across GCMs but for a given GCM changes modestly with time; a symmetric polar amplification index changes from the first decade to years 701–800 or (if available) years 2901–3000 by −6% to +8% in 6 of 12, increases by 34% in 1 outlier, and increases by 13%–22% in the remaining 5. The antisymmetric component weakens in time in all 12, but this varies considerably across GCMs—near-equilibrium warming is appreciably antisymmetric in some including FAMOUS versus almost entirely symmetric in some including CESM1. Based on these results, we consider a weak change to modest increase in symmetric polar amplification and modest to complete reduction in antisymmetric polar amplification to be robust responses and subsequently attempt to better understand them.

An MEBM prescribed with ocean heat uptake and radiative feedback parameter (λ) fields inferred from four different time periods of the $4 \times CO_2$ CESM1 simulation captures the salient GCM behaviors. In additional MEBM simulations with the antisymmetric components of λ and ocean heat uptake either removed or amplified, despite the antisymmetric warming pattern changing drastically, the symmetric warming pattern hardly changes. Conversely, removing the meridional structure in λ (even with its global mean unchanged) causes three key changes: it reduces mean warming at each time period, it makes the warming pattern more polar amplified at each time period, and it weakens the increase in time of the symmetric polar amplification index. Of these three, the first two are a straightforward consequence of λ being less stabilizing overall at high than low latitudes. The third, we argue, results from the loss after the initial decade of a deep global minimum in λ just equatorward of the Southern Ocean. This imprints onto the symmetric component of λ, and with no comparable change at lower latitudes, the result is that radiative restoring becomes comparatively less stabilizing in the extratropics than tropics, promoting polar amplification.

To clarify causes of differences across the GCMs, a simple three-box, two-time-scale model of warming in the Arctic, Antarctic, and lower-latitude sectors was fitted to 3000-yr time series of annual-mean surface warming in the end-member models CESM1 and FAMOUS. Strikingly, in FAMOUS there is effectively no difference in the fast response time scale between the Antarctic and elsewhere. This runs counter to CESM1 where the Antarctic time scale is an order of magnitude larger and to physical intuition given the delaying effect of Southern Ocean upwelling. Fortuitously, however, it enables an analytical approximate solution that yields a time-invariant symmetric polar amplification index in reasonably good agreement with the GCM.

Finally, we investigate the sensitivity of these behaviors to the radiative forcing via additional CESM1 simulations. The normalized symmetric warming pattern varies moderately across CO_2 magnitudes from 2 to 16 times preindustrial, with symmetric polar amplification increasing—and antisymmetric polar amplification decreasing—less in time the higher CO_2 is. At least after the first decade, both components change even less in time in a simulation generating an early Pliocene-like surface climate attained through meridionally patterned cloud albedo perturbations. Thus, qualitatively the symmetric component is insensitive in time and to forcing magnitude for a given forcing structure despite, unsurprisingly, depending sensitively on the forcing structure.

b. Discussion

Does the hemispherically symmetric/antisymmetric decomposition of polar-amplified warming add value over more conventional analyses? In terms of the bulk amplification indices defined as the ratio of polar cap-averaged warming to globally averaged warming, admittedly the results are mixed. Across the 12 GCMs under abrupt $4 \times CO_2$, the Arctic amplification index spans 1.79–2.50 in the first decade and changes afterward by −0.53 to +0.04—a larger range than that of PA_{sym} (−0.10 to +0.40) in absolute terms but actually smaller in percentage terms (−23% to +2% for the Arctic versus −6% to +34% for PA_{sym}). The Antarctic amplification index in the first decade spans 0.33–1.15 and changes thereafter from +0.04 to +1.27 (fractionally, +4% to +352%), a larger range than the first-to-last-period change in PA_{asym} of −0.09 to −0.90 (fractionally, −17% to −109%). As such, a complementary view would be that the robust responses are a weak change to modest decrease in Arctic amplification and a weak to large increase in Antarctic amplification. In either case, it is clear that model diversity in evolution of warming patterns across time scales is greatest for the southern extratropics, weakest in the tropics, and intermediate for the northern extratropics.

Further support for the southern high latitudes figuring centrally in model disagreement comes from the three-box, two-time-scale model fitted to the two end members FAMOUS and CESM1. Their most salient discrepancies are the ~5.5-fold longer Antarctic fast-response time scale

in CESM1 and the ~2.5–4.5-times-longer slow-response time scales in all regions for CESM1. Both involve ocean dynamical processes—prevailing Southern Ocean upwelling and deep ocean equilibration—suggesting a predominant role for ocean model formulation.

Nevertheless, going beyond scalar amplification indices to the full latitude-by-latitude pattern, by eye from Figs. 2, 3, and 9 clearly the mean-normalized symmetric component persists more in time from its values in initial decades over subsequent centuries and millennia than either the full field or its antisymmetric counterpart—and likewise (in CESM1 at least) across CO_2 concentrations. We therefore argue that the hemispherically symmetric/antisymmetric decomposition merits further study.

One useful next step would be extending the analyses to additional, higher resolution, and more modern GCMs via the CMIP6 abrupt $4 \times CO_2$ simulations—consider that the endmembers CESM1 and FAMOUS are both low-resolution and/or simplified versions of CMIP5-class GCMs. The CMIP abrupt $4 \times CO_2$ runs typically span 150 years, precluding direct investigation of the multi-centennial and longer time-scale behaviors. However, for the 12 GCMs we analyze, values in years 21–100 are well correlated with those for years 701–800 for global mean warming ($r = 0.99$), Arctic amplification ($r = 0.94$), Antarctic amplification ($r = 0.78$), PA_{sym} ($r = 0.87$), and PA_{asym} ($r = 0.84$).

Though constraining global-mean warming $\overline{T}$ at any given time scale is not our main focus, we find noteworthy its spread across the 12 GCMs. Near-equilibrium warming in the least sensitive model (GISSE2R) is surpassed within decades in half of the models. Conversely, the most sensitive model (FAMOUS) warms more in the first century than 10 of the other 11 do by years 701–800 and three of the other four do by years 2901–3000. In addition, the warming in the initial decade is well correlated with the millennial-time-scale warming: $r = 0.88$ between $\overline{T}$ in years 1–10 versus 701–800, and $r = 0.91$ for years 1–10 versus 2901–3000—raising the prospect of constraining mean warming over millennial time scales based on its rapidity on decadal time scales.

The MEBM simulations suggest that, in CESM1 at least, T^*_{sym} does not change dramatically after the first decade because the spatial structure of the radiative feedback parameter itself hardly varies after the first decade. How relevant this is to the real climate depends on the ability of GCMs to represent the presence (or in the case of CESM1, absence) of any state-dependent feedbacks that could result in regional changes in the radiative feedback parameter in time as mean warming increases. At least in the MEBM, making the radiative feedback parameter uniform—even with its global mean intact—considerably reduces climate sensitivity. It is well known that the evolving feedback field tends to increase sensitivity with time, but this is often understood in regard to its global-mean value becoming less stabilizing. In other words, the MEBM suggests that state-dependent climate sensitivity is related to having nonuniform feedbacks.

The ultimate motivation for this work is to infer as much as possible regarding anthropogenic climate change in the real climate system from limited data records. What can be inferred from the real climate system based on these results, bracketing temporarily questions of validity? Historical radiative forcing is characterized by two factors we have yet to consider. First is a gradual rather than abrupt CO_2 increase. A useful starting place would be standard 1% per year CO_2 increase simulations. In initial years to decades when the radiative forcing is still relatively small, global-mean warming will likely be too small for the mean-normalized fields to be meaningful, and the spatial pattern of warming will likely be strongly influenced by internal variability. For that reason, analyzing these fields in one or more available large ensembles could be useful. Second is a complex spatiotemporal evolution with nontrivial antisymmetric component owing to anthropogenic aerosols, volcanoes, and land-use change. We have not examined forcings with large hemispherically antisymmetric components, and it is possible that the T^*_{sym} and T^*_{asym} behaviors under such forcings would differ from the robust behaviors we have shown under predominantly symmetric forcing.

The 2–16 $\times CO_2$ simulation results from CESM1 suggest that, in that model at least, the T^*_{sym} and PA_{sym} behaviors are reasonably insensitive to CO_2 values ranging from 2 to 16× preindustrial, though with PA_{sym} moderately increasing with CO_2, while T^*_{asym} and PA_{asym} become more weighted to the Arctic as CO_2 increases. This helps contextualize the near vanishing of T^*_{asym} and PA_{sym} under $4 \times CO_2$: this is not intrinsic to CO_2-forced warming; rather $4 \times CO_2$ happens to be the amount at which the processes controlling the difference between the caps have comparable strengths. The $2 \times CO_2$ simulation is the only one in which Southern Hemisphere sea ice does not disappear entirely; under $16 \times CO_2$ it is nearly gone by years 21–100, under $8 \times CO_2$ by years 701–800, and under $4 \times CO_2$ by years 2901–3000 (not shown). Given the importance of sea ice loss in the severity of polar amplification (e.g., Dai et al. 2019), this likely contributes to the $2 \times CO_2$ being least like the others regarding the fields of our interest. Heede et al. (2020), analyzing nearly identical abrupt CO_2-increase simulations (in the same model, though run for only 500 years and with five ensemble members each), discuss in detail the ways in which the $2 \times CO_2$ simulation differs from the larger-magnitude CO_2 increase simulations.

We conclude by noting that this analysis depended crucially on the existence of an ensemble of millennial-scale integrations in LongRunMIP (Rugenstein et al. 2019), and that, in attempting to bound longer-time-scale behaviors from shorter integrations, it complements ongoing efforts such as the "fast-forward" technique (Saint-Martin et al. 2019) to attain equilibrium solutions in GCMs more rapidly.

Acknowledgments. We thank William Wang for generating several figures that facilitated our analyses. S.A.H. was supported during different periods of this study by an NSF Atmospheric and Geospace Sciences Postdoctoral Research Fellowship (NSF Award 1624740), a Caltech Foster and Coco Stanback Postdoctoral Fellowship, and a Columbia University Earth Institute Fellowship. T.M.M acknowledges support from NSERC. N.J.B. acknowledges support from NSF Award 1844380 and is supported by the Alfred P. Sloan

Foundation as a Research Fellow. A.V.F. acknowledges support from the ARCHANGE project (ANR-18-MPGA-0001, France). Three anonymous reviewers provided extremely useful comments and motivated the analyses of LongRunMIP and the box model.

APPENDIX

Moist Energy Balance Model Formulation

For the CO_2 radiative forcing [$\mathscr{F}(\varphi)$] we use the spatially varying instantaneous forcing of Huang et al. (2016) computed for a doubling of CO_2. This will not be identical to the radiative forcing computed with our particular GCM due to dependencies on the climatology (e.g., Merlis 2015; Huang et al. 2017). We convert this instantaneous $2 \times CO_2$ radiative forcing into a stratosphere-adjusted $4 \times CO_2$ radiative forcing by doubling it and then adding 2.4 W m^{-2} uniformly to yield a conventional global-mean value of 7.0 W m^{-2}. It is shown in Fig. 7a and is identical across all MEBM simulations presented.

The feedback parameter λ is diagnosed this radiative forcing field and fields taken from the GCM $4 \times CO_2$ simulation:

$$\lambda(\varphi) = -\frac{\mathscr{F}(\varphi) - \mathscr{T}(\varphi)}{T_{\text{gcm}}(\varphi)}, \tag{A1}$$

where $\mathscr{T}$ is the anomalous TOA radiative flux in the GCM (signed positive downward), and T_{gcm} is the anomalous surface air temperature in the GCM. The "gcm" subscript is meant to emphasize that the temperature field in the denominator of (A1) is that diagnosed from the GCM, not the MEBM's own computed temperature (whereas the temperature field that λ multiplies in (1) is that of the MEBM). One MEBM simulation is performed for each of the four time periods of interest, each with $\mathscr{T}$, T_{gcm}, and $\mathscr{O}$ taken from the CESM1 $4 \times CO_2$ simulation averaged over that time period.

For the diffusive approximation to atmospheric energy transport convergence, because all quantities are anomalies, surface MSE is linearized as $h = T(1 + \mathscr{H} L \partial_T q_{\text{sat}})/c_p$, with relative humidity $\mathscr{H}$, saturation specific humidity q_{sat}, and latent heat of vaporization L. The partial derivative of the saturation vapor pressure, $\partial_T q_{\text{sat}}$, is evaluated using the zonal-mean climatological surface air temperature from the GCM averaged over years 701–800 of the control simulation. The parameter values for all constant coefficients are standard: $\mathscr{H} = 0.8$, $\mathscr{D} = 0.3$ W m^{-2} K^{-1}, $c_p = 1004.6$ J kg^{-1} K^{-1}, and $L = 2.5 \times 10^6$ J kg^{-1}.

The MEBM is integrated to equilibrium using a fourth-order Runge–Kutta time-stepping scheme. A second-order finite difference scheme is used for the ∇^2 operator (Wagner and Eisenman 2015). There are 60 model grid points evenly spaced in $\sin\varphi \approx 1/30$ increments, with gridpoint centers in each hemisphere from $\sin\varphi \approx 0.12$ (corresponding to $\varphi \approx 4.8°$) to $\sin\varphi \approx 0.98$ (corresponding to $\varphi \approx 79.5°$). The CESM1 fields, which are evenly spaced in latitude over 48 boxes spanning ~1.8°–87.2° in each hemisphere with ~3.6° spacing, are spectrally transformed at order 20 to the MEBM grid.

REFERENCES

Alexeev, V. A., and C. H. Jackson, 2013: Polar amplification: Is atmospheric heat transport important? *Climate Dyn.*, **41**, 533–547, https://doi.org/10.1007/s00382-012-1601-z.

Andrews, T., J. M. Gregory, and M. J. Webb, 2015: The dependence of radiative forcing and feedback on evolving patterns of surface temperature change in climate models. *J. Climate*, **28**, 1630–1648, https://doi.org/10.1175/JCLI-D-14-00545.1.

Armour, K. C., C. M. Bitz, and G. H. Roe, 2013: Time-varying climate sensitivity from regional feedbacks. *J. Climate*, **26**, 4518–4534, https://doi.org/10.1175/JCLI-D-12-00544.1.

——, N. Siler, A. Donohoe, and G. H. Roe, 2019: Meridional atmospheric heat transport constrained by energetics and mediated by large-scale diffusion. *J. Climate*, **32**, 3655–3680, https://doi.org/10.1175/JCLI-D-18-0563.1.

Bonan, D. B., K. C. Armour, G. H. Roe, N. Siler, and N. Feldl, 2018: Sources of uncertainty in the meridional pattern of climate change. *Geophys. Res. Lett.*, **45**, 9131–9140, https://doi.org/10.1029/2018GL079429.

Burls, N. J., and A. V. Fedorov, 2014a: Simulating Pliocene warmth and a permanent El Niño-like state: The role of cloud albedo. *Paleoceanogr. Paleoclimatol.*, **29**, 893–910, https://doi.org/10.1002/2014PA002644.

——, and ——, 2014b: What controls the mean east–west sea surface temperature gradient in the equatorial Pacific: The role of cloud albedo. *J. Climate*, **27**, 2757–2778, https://doi.org/10.1175/JCLI-D-13-00255.1.

——, ——, D. M. Sigman, S. L. Jaccard, R. Tiedemann, and G. H. Haug, 2017: Active Pacific meridional overturning circulation (PMOC) during the warm Pliocene. *Sci. Adv.*, **3**, e1700156, https://doi.org/10.1126/sciadv.1700156.

Dai, A., D. Luo, M. Song, and J. Liu, 2019: Arctic amplification is caused by sea-ice loss under increasing CO_2. *Nat. Commun.*, **10**, 121, https://doi.org/10.1038/s41467-018-07954-9.

Danabasoglu, G., and P. R. Gent, 2009: Equilibrium climate sensitivity: Is it accurate to use a slab ocean model? *J. Climate*, **22**, 2494–2499, https://doi.org/10.1175/2008JCLI2596.1.

Ding, Q., J. M. Wallace, D. S. Battisti, E. J. Steig, A. J. E. Gallant, H.-J. Kim, and L. Geng, 2014: Tropical forcing of the recent rapid Arctic warming in northeastern Canada and Greenland. *Nature*, **509**, 209–212, https://doi.org/10.1038/nature13260.

Dong, Y., K. C. Armour, M. D. Zelinka, C. Proistosescu, D. S. Battisti, C. Zhou, and T. Andrews, 2020: Intermodel spread in the pattern effect and its contribution to climate sensitivity in CMIP5 and CMIP6 models. *J. Climate*, **33**, 7755–7775, https://doi.org/10.1175/JCLI-D-19-1011.1.

Fedorov, A. V., N. J. Burls, K. T. Lawrence, and L. C. Peterson, 2015: Tightly linked zonal and meridional sea surface temperature gradients over the past five million years. *Nat. Geosci.*, **8**, 975–980, https://doi.org/10.1038/ngeo2577.

Feldl, N., B. T. Anderson, and S. Bordoni, 2017: Atmospheric eddies mediate lapse rate feedback and Arctic amplification. *J. Climate*, **30**, 9213–9224, https://doi.org/10.1175/JCLI-D-16-0706.1.

Flannery, B. P., 1984: Energy balance models incorporating transport of thermal and latent energy. *J. Atmos. Sci.*, **41**, 414–421, https://doi.org/10.1175/1520-0469(1984)041<0414:EBMITO>2.0.CO;2.

Frierson, D. M. W., and Y.-T. Hwang, 2012: Extratropical influence on ITCZ shifts in slab ocean simulations of global warming. *J. Climate*, **25**, 720–733, https://doi.org/10.1175/JCLI-D-11-00116.1.

Geoffroy, O., and D. Saint-Martin, 2014: Pattern decomposition of the transient climate response. *Tellus*, **66A**, 23393, https://doi.org/10.3402/tellusa.v66.23393.

——, ——, D. J. L. Olivié, A. Voldoire, G. Bellon, and S. Tytéca, 2013: Transient climate response in a two-layer energy-balance model. Part I: Analytical solution and parameter calibration using CMIP5 AOGCM experiments. *J. Climate*, **26**, 1841–1857, https://doi.org/10.1175/JCLI-D-12-00195.1.

Heede, U. K., A. V. Fedorov, and N. J. Burls, 2020: Time scales and mechanisms for the tropical Pacific response to global warming: A tug of war between the ocean thermostat and weaker Walker. *J. Climate*, **33**, 6101–6118, https://doi.org/10.1175/JCLI-D-19-0690.1.

Held, I. M., M. Winton, K. Takahashi, T. Delworth, F. Zeng, and G. K. Vallis, 2010: Probing the fast and slow components of global warming by returning abruptly to preindustrial forcing. *J. Climate*, **23**, 2418–2427, https://doi.org/10.1175/2009JCLI3466.1.

Henry, M., T. M. Merlis, N. J. Lutsko, and B. E. J. Rose, 2021: Decomposing the drivers of polar amplification with a single-column model. *J. Climate*, **34**, 2355–2365, https://doi.org/10.1175/JCLI-D-20-0178.1.

Huang, Y., X. Tan, and Y. Xia, 2016: Inhomogeneous radiative forcing of homogeneous greenhouse gases. *J. Geophys. Res. Atmos.*, **121**, 2780–2789, https://doi.org/10.1002/2015JD024569.

——, Y. Xia, and X. Tan, 2017: On the pattern of CO_2 radiative forcing and poleward energy transport. *J. Geophys. Res. Atmos.*, **122**, 10 578–10 593, https://doi.org/10.1002/2017JD027221.

Hwang, Y.-T., D. M. W. Frierson, and J. E. Kay, 2011: Coupling between Arctic feedbacks and changes in poleward energy transport. *Geophys. Res. Lett.*, **38**, L17704, https://doi.org/10.1029/2011GL048546.

Jansen, M. F., L.-P. Nadeau, and T. M. Merlis, 2018: Transient versus equilibrium response of the ocean's overturning circulation to warming. *J. Climate*, **31**, 5147–5163, https://doi.org/10.1175/JCLI-D-17-0797.1.

Li, C., J.-S. von Storch, and J. Marotzke, 2013: Deep-ocean heat uptake and equilibrium climate response. *Climate Dyn.*, **40**, 1071–1086, https://doi.org/10.1007/s00382-012-1350-z.

Manabe, S., R. J. Stouffer, M. J. Spelman, and K. Bryan, 1991: Transient responses of a coupled ocean–atmosphere model to gradual changes of atmospheric CO_2. Part I: Annual mean response. *J. Climate*, **4**, 785–818, https://doi.org/10.1175/1520-0442(1991)004<0785:TROACO>2.0.CO;2.

Marshall, J., J. R. Scott, K. C. Armour, J.-M. Campin, M. Kelley, and A. Romanou, 2015: The ocean's role in the transient response of climate to abrupt greenhouse gas forcing. *Climate Dyn.*, **44**, 2287–2299, https://doi.org/10.1007/s00382-014-2308-0.

Merlis, T. M., 2015: Direct weakening of tropical circulations from masked CO_2 radiative forcing. *Proc. Natl. Acad. Sci. USA*, **112**, 13 167–13 171, https://doi.org/10.1073/pnas.1508268112.

——, and M. Henry, 2018: Simple estimates of polar amplification in moist diffusive energy balance models. *J. Climate*, **31**, 5811–5824, https://doi.org/10.1175/JCLI-D-17-0578.1.

Previdi, M., T. P. Janoski, G. Chiodo, K. L. Smith, and L. M. Polvani, 2020: Arctic amplification: A rapid response to radiative forcing. *Geophys. Res. Lett.*, **47**, e2020GL089933, https://doi.org/10.1029/2020GL089933.

Roe, G. H., N. Feldl, K. C. Armour, Y.-T. Hwang, and D. M. W. Frierson, 2015: The remote impacts of climate feedbacks on regional climate predictability. *Nat. Geosci.*, **8**, 135–139, https://doi.org/10.1038/ngeo2346.

Rohrschneider, T., B. Stevens, and T. Mauritsen, 2019: On simple representations of the climate response to external radiative forcing. *Climate Dyn.*, **53**, 3131–3145, https://doi.org/10.1007/s00382-019-04686-4.

Rose, B. E. J., K. C. Armour, D. S. Battisti, N. Feldl, and D. D. B. Koll, 2014: The dependence of transient climate sensitivity and radiative feedbacks on the spatial pattern of ocean heat uptake. *Geophys. Res. Lett.*, **41**, 1071–1078, https://doi.org/10.1002/2013GL058955.

Rugenstein, M., and Coauthors, 2019: LongRunMIP: Motivation and design for a large collection of millennial-length AOGCM simulations. *Bull. Amer. Meteor. Soc.*, **100**, 2551–2570, https://doi.org/10.1175/BAMS-D-19-0068.1.

——, and Coauthors, 2020: Equilibrium climate sensitivity estimated by equilibrating climate models. *Geophys. Res. Lett.*, **47**, e2019GL083898, https://doi.org/10.1029/2019GL083898.

Russotto, R. D., and M. Biasutti, 2020: Polar amplification as an inherent response of a circulating atmosphere: Results from the TRACMIP aquaplanets. *Geophys. Res. Lett.*, **47**, e2019GL086771, https://doi.org/10.1029/2019GL086771.

Saint-Martin, D., and Coauthors, 2019: Fast-forward to perturbed equilibrium climate. *Geophys. Res. Lett.*, **46**, 8969–8975, https://doi.org/10.1029/2019GL083031.

Senior, C. A., and J. F. B. Mitchell, 2000: The time-dependence of climate sensitivity. *Geophys. Res. Lett.*, **27**, 2685–2688, https://doi.org/10.1029/2000GL011373.

Shields, C. A., D. A. Bailey, G. Danabasoglu, M. Jochum, J. T. Kiehl, S. Levis, and S. Park, 2012: The low-resolution CCSM4. *J. Climate*, **25**, 3993–4014, https://doi.org/10.1175/JCLI-D-11-00260.1.

Shin, Y., and S. M. Kang, 2021: How does the high-latitude thermal forcing in one hemisphere affect the other hemisphere? *Geophys. Res. Lett.*, **48**, e2021GL095870, https://doi.org/10.1029/2021GL095870.

Smith, R. S., J. M. Gregory, and A. Osprey, 2008: A description of the FAMOUS (version XDBUA) climate model and control run. *Geosci. Model Dev.*, **1**, 53–68, https://doi.org/10.5194/gmd-1-53-2008.

Stephens, G. L., D. O'Brien, P. J. Webster, P. Pilewski, S. Kato, and J.-l. Li, 2015: The albedo of Earth. *Rev. Geophys.*, **53**, 141–163, https://doi.org/10.1002/2014RG000449.

Stuecker, M. F., and Coauthors, 2018: Polar amplification dominated by local forcing and feedbacks. *Nat. Climate Change*, **8**, 1076–1081, https://doi.org/10.1038/s41558-018-0339-y.

Tebaldi, C., and J. M. Arblaster, 2014: Pattern scaling: Its strengths and limitations, and an update on the latest model simulations. *Climatic Change*, **122**, 459–471, https://doi.org/10.1007/s10584-013-1032-9.

Virtanen, P., and Coauthors, 2020: SciPy 1.0: Fundamental algorithms for scientific computing in Python. *Nat. Methods*, **17**, 261–272, https://doi.org/10.1038/s41592-019-0686-2.

Voigt, A., B. Stevens, J. Bader, and T. Mauritsen, 2013: The observed hemispheric symmetry in reflected shortwave irradiance. *J. Climate*, **26**, 468–477, https://doi.org/10.1175/JCLI-D-12-00132.1.

——, ——, ——, and ——, 2014: Compensation of hemispheric albedo asymmetries by shifts of the ITCZ and tropical clouds. *J. Climate*, **27**, 1029–1045, https://doi.org/10.1175/JCLI-D-13-00205.1.

Wagner, T. J. W., and I. Eisenman, 2015: How climate model complexity influences sea ice stability. *J. Climate*, **28**, 3998–4014, https://doi.org/10.1175/JCLI-D-14-00654.1.